Spatial and temporal variations in basal melting at Nivlisen ice shelf, East Antarctica, derived from phase-sensitive radars

Katrin Lindbäck[1], Geir Moholdt[1], Keith W. Nicholls[2], Tore Hattermann[1], Bhanu Pratap[3], Meloth Thamban[3], Kenichi Matsuoka[1]

[1] Norwegian Polar Institute, Framsentret, Postboks 6606, Langnes, 9296 Tromsø, Norway.

[2] British Antarctic Survey, Natural Environmental Research Council, High Cross, Madingley Rd, Cambridge CB3 0ET, UK.

[3] ESSO-National Centre for Polar and Ocean Research, Ministry of Earth Sciences, Headland Sada, Vasco-da-Gama, Goa 403 804, India.

Correspondence to: Katrin Lindbäck (katrin.lindback@npolar.no)

Abstract

Thinning rates of ice shelves vary widely around Antarctica and basal melting is a major component in ice shelf mass loss. In this study, we present records of basal melting, at unique spatial and temporal resolution for East Antarctica, derived from autonomous phase-sensitive radars. These records show spatial and temporal variations of basal melting in 2017 and 2018 at Nivlisen ice shelf, central Dronning Maud Land. The annually averaged basal melt rates are in general moderate (~0.8 m yr^{-1}). Radar profiling of the ice-shelf shows variable ice thickness from smooth beds to basal crevasses and channels. The highest basal melt rates (3.9 m yr^{-1}) were observed close to a grounded feature near the ice shelf front. Daily time-varying measurements reveal a seasonal melt signal 4 km from the ice shelf front, at an ice draft of 130 m, where the highest daily basal melt rates occurred in summer (up to 5.6 m yr^{-1}). In comparison with wind, air temperatures, and sea-ice cover from reanalysis and satellite data the seasonality in basal melt rates indicates that summer-warmed ocean surface water was pushed by wind beneath the ice

26   shelf front. We observed a different melt regime 35 km into the ice-shelf cavity, at an ice draft of

27   280 m, with considerably lower basal melt rates (annual average of 0.4 m yr^{-1}) and no

28   seasonality. We conclude that warm deep ocean water at present has limited effect on the basal

29   melting of Nivlisen. On the other hand, a warming in surface waters, as a result of diminishing

30   sea-ice cover has the potential to increase basal melting near the ice-shelf front. Continuous in

31   situ monitoring of Antarctic ice shelves is needed to understand the complex mechanisms

32   involved in ice shelf–ocean interactions.

33

34   **1   Introduction**

35   The Antarctic contribution to global sea-level rise has increased by a factor of five in the

36   past two decades (The IMBIE Team, 2018). Over 80 % of the grounded ice in Antarctica drains

37   out into floating ice shelves (Dupont and Alley, 2005). The thinning rates of these ice shelves

38   vary widely around the continent (Paolo et al., 2015). The mass balance of an ice shelf is the sum

39   of the ice gain and loss; ice gain comprises the advective input from ice across the grounding

40   zone (where ice detaches from the bed and becomes afloat), snow accumulation, and marine ice

41   accretion. Ice loss encompasses surface melting and sublimation, basal melting from the ocean

42   underneath the floating ice shelf, and iceberg calving at the ice front (Bamber et al., 2018). A

43   negative mass balance can affect ice-shelf stability: where a net mass loss reduces back stresses

44   on grounded ice upstream, leading the tributaries to flow faster (Reese et al., 2018).

45   Understanding controls on the mass balance of ice shelves around Antarctica is therefore the key

46   to gain a better understanding of the continent's present and future contribution to global sea-

47   level rise.

48   Iceberg calving occurs irregularly in time and can have dramatic effects on ice shelf mass

49   balance when it occurs (Hogg and Gudmundsson, 2017). At present, iceberg calving comprises

50   approximately half of the mass loss from the Antarctic Ice Sheet, where the other half comes

51   from basal melting (Depoorter et al., 2013; Rignot et al., 2013). Basal melting is not uniform and

52   depends on the ocean properties in the vicinity of the ice shelf, the topography of both the ocean

53   bed. and the ice-shelf base. Jacobs et al. (1992) described how different water masses can melt

54   the ice shelf from below:

55   In mode 1, ocean water with temperatures at the surface freezing point provides heat for

56   melting of deeper parts of the ice base, because the pressure-melting point of the ice is decreased

57   to lower temperatures at depth. Basal melting at the deep grounding zones can be high and often

58   occur at basal channels (e.g., 22 m yr^{-1} for Ross Ice Shelf; Marsh et al., 2016); however,

59   substantial marine-ice accretion reduces the net melting below these large ice shelves when the

60   rising melt plume from the grounding zone super-cools and refreezes on the ice-shelf base at

61   shallower depths (Joughin and Vaughan, 2004). Since these cold shelf waters provide a limited

62   source of ocean heat (Darelius and Sallée, 2017), average basal melt rates are often low for the

63   largest ice shelves (e.g., 0.3 m yr^{-1} for Ronne Ice Shelf; Rignot et al., 2013).

64   In mode 2, ice shelves melt from the presence of warm circumpolar deep water intrusion

65   (Jacobs et al., 1992). The rapid retreat and high thinning rates of glaciers in Antarctica have been

66   attributed to the presence of warm circumpolar deep water below ice shelves in the Amundsen

67   Sea sector of West Antarctica (Pritchard et al., 2012; Rignot et al., 2013). Circumpolar deep

68   water surrounds the Antarctic continent, flowing clockwise with the Antarctic Circumpolar

69   Current and is abundant near the continental shelf of West Antarctica. Circumpolar deep water

70   accesses the deep bases of ice shelves directly through cross-continental submarine troughs,

71   causing the higher basal melt rates; for example Rignot et al. (2013) found Pine Island Ice Shelf

72   to have an average melt rate of 16 m yr^{-1}. In East Antarctica, basal melting has been linked to

73   circumpolar deep water intrusion only at Totten Ice Shelf, where annual basal melt rates reached

74   ~11 m yr^{-1} (Rignot et al., 2013; Rintoul et al., 2016). Farther west, in the Weddell Sea sector a

75   cooler modified version of circumpolar deep water is advected along the coast (Dong et al.,

76   2016; Ryan et al., 2016).

77   In mode 3, ice shelves can melt at shallow depths in the vicinity of their ice fronts when

78   summer-warmed surface water is pushed by wind and tides under ice shelves (Jenkins and

79   Doake, 1991; Makinson and Nicholls, 1999; Sverdrup, 1954; Zhou et al., 2014). Antarctic

80   surface water has been observed under the Ross Ice Shelf in West Antarctica (Malyarenko et al.,

81   2019; Stern et al., 2013; Stewart et al., 2019) and at Fimbulisen in East Antarctica (Hattermann

82   et al., 2012), suggesting it may be a more important process in basal melting than previously

83   thought. Spatial patterns and relative magnitudes of all these three modes of basal melting
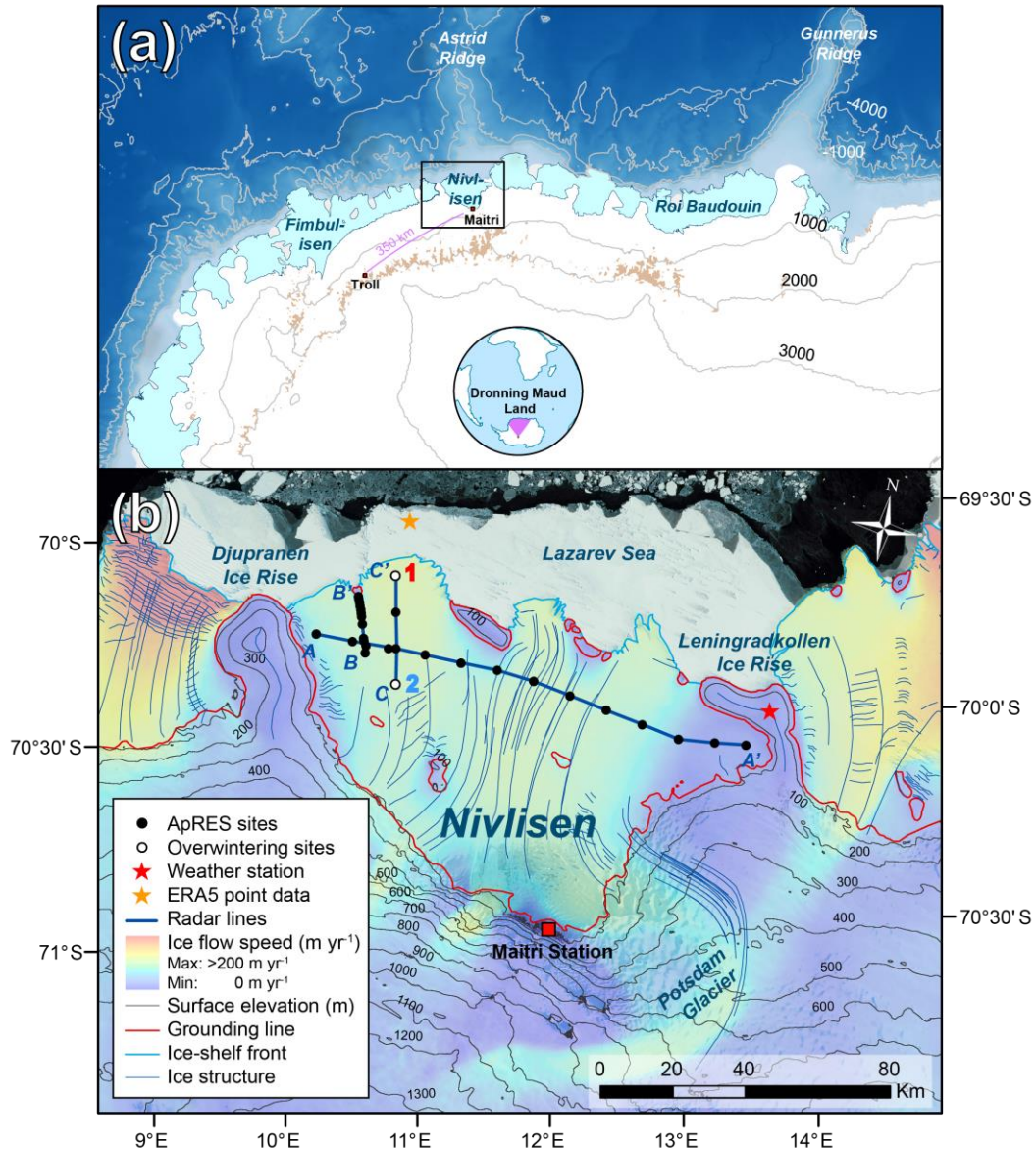
Figure 1. Study area: **(a)** Dronning Maud Land coast, with research stations, ice shelves (light blue), and elevation contours with bathymetric features (Arndt et al., 2013). **(b)** Nivlisen ice shelf with surrounding areas. Study sites, where ApRES and stakes for ice velocity and surface mass balance were located, ApRES overwintering sites (no. 1 called "seaward" and no. 2 called "landward"), and low-frequency radar profiles (A, B, and C). Satellite derived ice speed (Rignot et al., 2011), surface elevation (m a.s.l.; Howat et al., 2019), grounding line, ice-shelf front (Mouginot et al., 2017), and ice structure (Goel et al., in review) are also shown. Background image is Landsat image mosaic with sea ice in front of the ice shelf (Bindschadler et al., 2008). Grid coordinate system is WGS-84.

93   remain largely unknown. Numerical modelling, however, indicates that the response of basal

94   melting in the future strongly depends on the surface air warming (Kusahara and Hasumi, 2013).

95   Future basal melting in Antarctica will therefore reflect the integrated response to changes in

96   circumpolar deep water temperatures and coastal processes that control its access onto the

97   continental shelf (Thompson et al., 2018). The detailed interplay of these processes today and in

98   a future climate are still a major source of uncertainty when evaluating the response of the

99   Antarctic Ice Sheet to climate change (Adusumilli et al., 2018).

100   In this study, we measured basal melting at Nivlisen (70° S, 12° E) in central Dronning

101   Maud Land, East Antarctica, using autonomous phase-sensitive radio-echo sounders (ApRES;

102   Fig. 1). Phase-sensitive radars use a technique where the phase of individual internal ice

103   reflectors is tracked, yielding time series of ice thickness change at high accuracy (~1 mm) and

104   short time intervals (Corr et al., 2002; Nicholls et al., 2015). This technique has been used to

105   measure basal and englacial properties of ice at several locations around Antarctica (e.g., Davis

106   et al., 2018; Jenkins et al., 2006; Marsh et al., 2016; Stewart et al., 2019) and in Greenland

107   (Vaňková et al., 2018). Our objective is to study the spatial and temporal variations of basal

108   melting and to interpret the results using: (1) radar profiles of ice thickness, (2) in situ measured

109   and satellite-derived or modelled ice flow speed and surface mass balance, and (3) atmospheric

110   forcing from reanalysis data, sea-ice distribution, and ocean tides. The data imply that different

111   modes of basal melting are present at Nivlisen. Our in situ measured data of basal melting

112   complement satellite-derived maps of spatially-smoothed time-averaged basal melt rates, and

113   will be a valuable data source for validation of ice shelf and ocean models.

114

115   **2   Study area**

116   Dronning Maud Land covers a large area of East Antarctica, and its 2000 km-long coast

117   is characterized by extensive ice shelves interspersed with numerous ice rises and rumples (Fig.

118   1a). Ice rises are locations where ice-shelf flow is diverted around the grounded ice and are

119   miniature ice caps with their own flow fields from the summit (Matsuoka et al., 2015). Ice

120   rumples are smaller features that impose a disturbance on the ice-shelf flow, causing the ice to

121   thicken upstream with extensive crevassing. Individual ice shelves are relatively small, but

122 extend close to, or even beyond, the continental-shelf break (Heywood et al., 1998). Basal melt

123 rates from satellite data in Dronning Maud Land vary from near zero to 7 m yr^{-1} (2003 to 2008;

124 Rignot et al., 2013). The interior of this region is partly separated by high mountains, causing

125 steep ice surface slopes from the continental plateau towards the coastal areas (Howat et al.,

126 2019). The drainage basin of Nivlisen (27 700 km^2), including the grounded ice that drains to the

127 ice shelf, has an estimated potential of raising global sea level by 8 cm (Rignot et al., 2019).

128   Nivlisen has an areal extent of ~7300 km^2 and forms a closed embayment between two

129 larger promontory-type ice rises, Djupranen and Leningradkollen (Fig. 1b). Such grounded

130 features are known to play vital roles in ice-shelf and ice-sheet dynamics over various

131 timescales. For example, un-grounding of an ice rumple within the ice shelves of Pine Island and

132 Thwaites Glacier is thought to be a major cause of the ongoing rapid retreat and thinning (Favier

133 et al., 2012; Gladstone et al., 2012; Jenkins et al., 2010). Bawden Ice Rise near the edge of the

134 Larsen C Ice Shelf helps maintain its stability, despite the collapse of neighbouring Larsen A and

135 B ice shelves (Borstad et al., 2013; Holland et al., 2015). Nivlisen is grounded at a series of

136 smaller ice rises and rumples near the present ice front, as well as at a few ice rumples in the

137 middle of the ice shelf (Moholdt and Matsuoka, 2015). The bathymetry under the ice shelf is

138 unknown.

139   The average ice shelf flow speed is 80 m yr^{-1} (Rignot et al., 2011). Potsdam Glacier

140 drains into Nivlisen from the southeast, with an average ice thickness of ~1000 m (Fretwell et

141 al., 2013) and ice flow speed of ~50 m yr^{-1} (Anschütz et al., 2007; Rignot et al., 2011). The

142 satellite-derived estimate of the grounding-line flux for Nivlisen was 3.9 ± 0.8 Gt yr^{-1}

143 (2007−2008; Rignot et al., 2013). Elevated topography of the ice rises causes highly-variable

144 local climate and surface mass balance gradients (Lenaerts et al., 2014). In addition, Nivlisen has

145 large surface mass balance transitions from being positive in the firn area near the ice front to

146 being negative in the blue-ice area near the grounding zone, with increased wind erosion,

147 evaporation, and sublimation owing to katabatic winds (Horwath et al., 2006). Near the

148 grounding zone, summer surface melting is sufficient to form supraglacial lakes and streams that

149 may occasionally drain through the ice shelf (Kingslake et al., 2015), making Nivlisen

150 potentially sensitive to hydrofracturing (Lenaerts et al., 2017). Rignot et al. (2013) estimated the

151 surface mass balance to be 1.8 ± 0.3 Gt yr^{-1} (average 1979–2010) and the average calving flux to

152 be 1.3 ± 0.4 Gt yr^{-1} (2007−2008). These numbers together with the grounding-line flux

153 mentioned earlier and a slightly positive net mass balance of 0.6 Gt yr^{-1} (2003−2008) results in a

154 residual net basal melt of 3.9 Gt yr^{-1}, or an average basal melt rate of 0.5 ± 0.2 m yr^{-1} (Rignot et

155 al., 2013). Thus, basal melting comprises ~75 % of the total outgoing flux, with the residual ~25

156 % attributed to iceberg calving.

157   The continental shelf extends ~100 km north of Nivlisen into the Lazarev Sea, and is

158 roughly 500 m deep (Arndt et al., 2013; Fig. 1a). Carbon dating of laminated sediments on

159 several locations near the ice shelf suggests that the ice front retreated to its present position by

160 ~11 kyr ago (Gingele et al., 1997). North of Nivlisen lies Astrid Ridge (Fig. 1a), an undersea

161 bathymetric feature extending from the Antarctic margin northward to ~65° S. Farther east lies

162 Gunnerus Ridge (Fig. 1a), where circumpolar deep water is entrained into the Antarctic slope

163 current. The circumpolar deep water is then cooled and modified to become warm deep water

164 (Dong et al., 2016; Ryan et al., 2016) and flows westward along the continental slope to finally

165 become entrained into the Weddell Gyre. The ice-shelf cavities in this region are separated from

166 warm deep water by the Antarctic slope front, which is a pronounced transition zone over the

167 narrow continental shelf between eastern shelf water and warm deep water. The slope front is

168 mainly attributed to coastal downwelling caused by the prevailing easterly winds (Sverdrup,

169 1954; Thompson et al., 2018). The coastal dynamics that set the warm deep water depth along

170 the continental-shelf break involves the balance between wind-driven Ekman overturning and

171 counteracting eddy fluxes (Nøst et al., 2011; Thompson et al., 2014). These processes respond to

172 changes in wind and buoyancy fluxes (Hattermann et al., 2014; Stewart and Thompson, 2016),

173 including self-amplifying feedbacks of increased fresh water input from increased basal melting

174 (Hattermann, 2018).

175   The Southern Ocean, including the Weddell Sea, has warmed over recent decades (Gille,

176 2002; Schmidtko et al., 2014) with the changes driven primarily by anthropogenic climate

177 warming (Swart et al., 2018). Sea-ice cover has increased slightly since 1979 around Antarctica

178 in general (De Santis et al., 2017), however extreme changes have occurred in recent years with

179 record maxima three years in a row (2012 to 2014), followed by record minima 2016 and 2017

180   (Shepherd et al., 2018; Stuecker et al., 2017; Turner et al., 2015). Sea-ice fluctuations are

181   strongly correlated with the dominant trends in Southern Hemisphere climate variability (Kwok

182   et al., 2016; Kwok and Comiso, 2002), although further studies are needed to understand the

183   drivers behind these fluctuations (Turner 2017). An increase in the seasonality of the easterly

184   winds has been observed (Hazel and Stewart, 2019) and this may affect the formation and export

185   of sea ice and the transport of surface waters and warm deep water to the continental shelf. All

186   these pan-Antarctic observations may affect ocean water flow and consequent ice-shelf thinning

187   in Dronning Maud Land and remains largely unknown.

188

3   Data and Methods

190   We conducted three field campaigns on Nivlisen and adjacent ice rises during the

191   Antarctic austral summers, from mid-November until end of December, 2016 to 2018, with

192   logistic support from the Indian Maitri and Norwegian Troll Station (Fig. 1a). In December

193   2016, we installed stakes for measurement of ice velocity and surface mass balance at 29

194   locations on Nivlisen and measured the ice thickness with an ApRES system (200–400 MHz),

195   developed by the British Antarctic Survey (British Antarctic Survey, 2018; Nicholls et al., 2015;

196   Fig. 1b): (A) 13 stakes were placed across the ice flow at a spacing of 10 km (profile A), (2) 10

197   stakes were placed along the ice flow towards a grounded feature near the ice front with a

198   spacing of 1 to 4 km (profile B), and (3) Four stakes were placed along the ice flow towards the

199   ice front at a spacing of 10 km (profile C). We also measured the ice-shelf thickness and basal

200   structure with a low-frequency (5 MHz) radio-echo sounder along these three profiles. After the

201   initial measurements, we installed similar ApRES systems at two locations for hourly

202   measurements of basal melting and strain rates over the winter, each powered by a 12 V 114 Ah

203   battery (Fig. 1b): (1) 4 km from the ice-shelf front, called the "seaward site" hereafter, and (2) 35

204   km from the ice shelf front, called the "landward site". In December 2017 and 2018, we revisited

205   and re-measured all ApRES sites to get averaged annual values of basal melting and strain rates

206   and retrieved the time-series data from the two overwintering stations. Extensive crevassing

207   prevented the three sites closest to the ice rumple (profile B, Fig. 1b) from being revisited in

208   2018.

3.1 Autonomous phase-sensitive radio echo sounder

ApRES uses the frequency-modulated continuous wave (FMCW) technique (Rahman, 2016). The instrument transmits a signal sweeping from 200–400 MHz over a period of 1 s to form a chirp (Nicholls et al., 2015). The system has a low-power consumption, with a power to the transmitter antenna of 100 mW. The averaged signal was amplified and de-ramped, a process where the received signal is mixed with a replica of the transmitted signal to extract differences in frequencies. The de-ramped signal was then filtered to amplify the higher frequencies preferentially, which enhanced weaker signals from more distant reflectors. Each sample consisted of 100 chirps, collected over a period of a few minutes. The data were digitized and stored on secure digital cards for further processing.

We processed the data following Brennan et al. (2014) and Nicholls et al. (2015). The data were Fourier transformed to give a complex signal amplitude as a function of delay time (or depth) assuming a constant propagation velocity of 168 m μs^{-1}. An amplitude cross correlation between the two returns, for a depth range within the firn layer (typically from 40 to 70 m), provided a vertical shift that approximately accounted for snow accumulation between the visits. The displacement of the reflectors between the two visits were then plotted as a function of depth (Supplements Fig. S1a). To give the necessary depth resolution, the phase of the signals was used to calculate the displacements by cross-correlating 4 m segments of the first profile with the complex conjugate of the corresponding segment of the second. Under the assumption of a constant vertical strain rate between the bottom of the firn layer and just above the ice base, we fit a straight line to the layer displacements. The correction for snow accumulation between the two visits included the coarse correction mentioned above and the precise correction inherent in the phase processing. This effect, together with the effect of the non-linear (with depth) displacements due to firn compaction, were contained within the intercept at the vertical axis. Thus the basal melt was given by the deviation of the displacement of the basal reflection from the straight line fit (Supplements Fig. S1b). The error in the calculated strain was estimated using the quality of fit of the linear regression. The uncertainty in the melt rate was obtained by combining the uncertainty in the strain rate with the uncertainty in the change in the range to the basal reflector, deduced from the signal-to-noise ratios of the two basal reflections.

238   To calculate the hourly melt rate time-series for the two overwintering sites (Fig. 1b), we

239   tracked the basal reflector using phase-coherent processing. This allowed us to determine the

240   speed of motion of the ice base with respect to the antenna, which we hereafter call the thinning

241   rate. To remove the component of ice-column vertical strain rate caused by tidal variations, we

242   filtered the basal vertical speeds with a 36 h low-pass filter. We then removed an annual average

243   vertical strain rate from the filtered basal motion, resulting in net basal melt rates. We assumed

244   that, at periods longer than 36 hours, the variability in strain rate is small compared with the

245   variability in basal melt rate.

246   3.2   Low-frequency radar profiling

247   We collected ~180 km of continuous radio-echo sounding profiles on Nivlisen to

248   measure ice thickness and englacial and basal structure (profiles A, B, and C; Fig. 1b). We used

249   a common-offset impulse radar system (Dowdeswell and Evans, 2004) based on the radar

250   developed by Matsuoka et al. (2012) and processing steps following Lindbäck et al. (2014). We

251   used half-wavelength dipole antennas with a 5 MHz centre frequency, using a Kentech impulse

252   transmitter with an average output power of 35 W. The transmitter and receiver systems were

253   mounted on two sleds and towed behind a snowmobile at a speed of $\sim$10 km h^{-1}. We positioned

254   the measurements using data from a code-phase global positioning system (GPS) receiver

255   mounted on the radar receiver box 20 m in front of the common mid-point of the antennas along

256   the travelled trajectory of the snowmobile. We post-corrected the height using the Canadian

257   precise point-processing service (CSRS-PPP; Natural Resources Canada, 2017) from a kinematic

258   carrier-phase dual-frequency GPS receiver mounted on the snowmobile. The radar

259   measurements had an average trace spacing of ~5 m.

260   Several corrections and filters were applied to the radar data: (1) dewow and bandpass

261   filters, to remove unwanted frequency components in the data, (2) depth-variable gain function,

262   and (3) normal move-out correction to correct for antenna separation, including adjusted travel

263   times for the trigger delay. The basal returns were digitized semi-automatically with a cross-

264   correlation picker at the first break of the bed reflection (Irving et al., 2007). We calculated ice

265   thickness from the picked travel times of the bed return using a constant radio-wave velocity of

266   168 m µs^{-1} for ice. We added a correction term of 2 m to account for the faster propagation in

267   the firn (Supplements Fig. S1c). The firn has a depth of ~50 m, derived from the ApRES internal

268   reflectors (Supplements Fig. S1c). To show the depth of the base of the ice shelf in the water

269   column we calculated the ice draft from the ice thickness by subtracting the surface elevation,

270   using an EIGEN-6C4 mean geoid height of 17 m (Förste et al., 2014). We estimated the error in

271   ice thickness by standard analytical error propagation methods (Lapazaran et al., 2016; Taylor,

272   1996), outlined in Lindbäck et al. (2018). The estimation included the error in the radar

273   acquisition and horizontal positioning error, where the radar acquisition errors comprised errors

274   in radio-wave velocity and two-way travel time. Velocity can vary spatially, depending mainly

275   on density. Errors in two-way travel time were estimated to be the range resolution, which is the

276   accuracy of the measurement of the distance between the antenna and the bed. The average radar

277   system error was estimated to 13.3 ± 1.2 m. The surface and base of the ice shelf is relatively

278   flat, giving very small vertical errors from horizontal positioning (0.1 ± 0.2 m). The total error in

279   ice thickness is presented together with the data in Sect. 4.

280   3.3   Ice flow and surface mass balance from stakes

281   Stake height over the surface was measured manually, and stake position was measured

282   for 15 minutes using carrier-phase dual-frequency GPS receivers at 1 s logging interval. The

283   stakes were revisited and measured in December 2017 and 2018. We processed the positions

284   statically using CSRS-PPP (Natural Resources Canada, 2017). Snow density was measured at

285   five locations on Nivlisen with an auger drill to a depth of 3 m and varied from 430–450 kg m^{-3}.

286   We used the average snow density of 440 kg m^{-3} and an ice density of 917 kg m^{-3} to calculate

287   the surface mass balance in ice equivalent. Ice flow velocity and surface mass balance were

288   compared with estimates from satellite data (Rignot et al., 2011) and regional atmospheric

289   modelling (van de Berg et al., 2006).

290
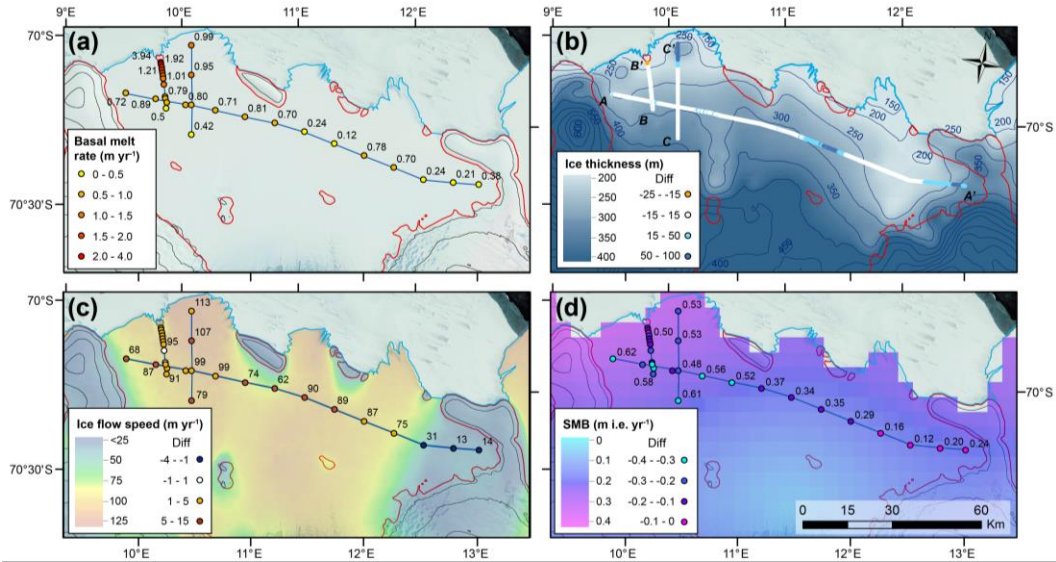
Figure 2. Comparison between in situ measured and satellite derived or modelled values: **(a)** ApRES-derived averaged annual basal melt rates. See Supplements Fig. S2 for averaged annual basal melt rates for 2018, which is on average within ±10 % from the 2017 values. **(b)** Ice thickness from Bedmap2 product (grid and contour lines; Fretwell et al., 2013) and difference to low-frequency radar profiles (satellite derived minus measured in point colour). **(c)** Ice flow speed from stakes (point numbers) and gridded satellite values (Rignot et al., 2011). Difference (satellite derived minus measured) are shown in point colour. **(d)** Surface mass balance (SMB) from stakes (point numbers) and gridded modelled values (van de Berg et al., 2006). Difference (modelled minus measured) are shown in point colour. Background image and contour lines are the same as in Fig. 1.

4   Results

In 2017, averaged annual basal melt rates, at 29 ApRES sites on Nivlisen (Fig. 1b), ranged from 0.12 ± 0.06 to 3.94 ± 0.04 m yr^{-1} (Fig. 2a and Fig. 3), with a median value of 0.80 m yr^{-1}. The highest averaged annual basal melt rates were observed just upstream of an ice rumple at the ice front. The lowest melt rates were observed in the central and eastern parts of the ice shelf. In 2018, averaged annual basal melt rates at 26 sites, ranged from 0.13 ± 0.06 to 1.48 ± 0.01 m yr^{-1} (Supplements Fig. S2). In 2018, the median melt rate was 0.72 m yr^{-1}. Basal melt rates were slightly lower in the second year at 18 sites and for 8 sites slightly higher. The measurements in 2018 excluded three sites closest to the ice rumple, which had the highest melt

310   rates in 2017, since we were not able to revisit these sites because of many crevasses in the area.

311   Errors in basal melt rates were on average 0.023 m yr^{-1} in 2017 and 0.025 m yr^{-1} in 2018.

312   Strain rates had a median averaged annual value of -4.7×10^{-4} yr^{-1} in 2017 and $-4.6 \times$

313   10^{-4} yr^{-1} in 2018. The vertical strain-rate contribution to the average rate of thickness change

314   was on average 22 %. The errors in strain were low, on average 6.2×10^{-5} yr^{-1} in 2017 and $7.1 \times$

315   10^{-5} yr^{-1} in 2018. For most parts of the ice shelf the strain rates were negative, meaning that the

316   ice was thinning by longitudinal stretching, however, close to the ice rumple mentioned earlier

317   (profile B; Fig. 3) we observed a transition from negative to positive strain rates (from $-5.4 \times$

318   10^{-4} to 2.2×10^{-2} yr^{-1}), with increasing compressional thickening of the ice towards the ice

319   rumple. Positive strain rates were also observed for five sites 5–10 km upstream of the larger ice

320   rises in the central and in the eastern part of the ice shelf (profile A; Fig. 3), indicating a far-

321   reaching buttressing effect (distance up to ~30 ice thicknesses from the ice rises).

322   The two overwintering ApRES systems were used to derive time series of basal melt

323   rates. The seaward overwintering site was located 4 km from the ice front and had an ice draft of

324   130 m, as measured with low-frequency radar. It operated for 14 months (from 11 Dec 2016–4

325   Feb 2018) before the battery failed. Thirty-six hour low-pass filtered basal melt rates at this site

326   varied from ~0 to 5.6 m yr^{-1}, where the highest melt rates occurred in summer (29 Jan 2017; Fig.

327   4a). The landward overwintering site was located 35 km from the ice front and had an ice draft

328   of 280 m. The data cover 22 months (from 4 Jan 2017–27 Nov 2018), excluding December 2017

329   when the instrument was used for measuring annual basal melt rates at other sites. At this site, 36

330   h low-pass filtered basal melt rates varied from ~0 to 2.0 m yr^{-1}, where the highest melt rates

331   occurred in winter (12 Jun 2018; Fig. 5a).

332   Ice thickness, measured with low-frequency radar along profiles A, B, and C (Fig. 1b),

333   varied from 160 to 330 m (Fig. 2b), with a median value of 260 m. We observed the thinnest ice

334   close to the ice front along profile C (Fig. 3) and the thickest ice in the southern-most part of the

335   ice shelf along the same profile. The total error in ice thickness along the profiles, including

336   radar system and positioning errors, varied between 10.6 and 15.7 m. The broad thickness pattern

337   agrees with the gridded ice thickness of Bedmap2 (Fretwell et al., 2013), except close to the ice

338   front in the western part (profile C), where the thickness of Bedmap2 is clearly too high (Fig.
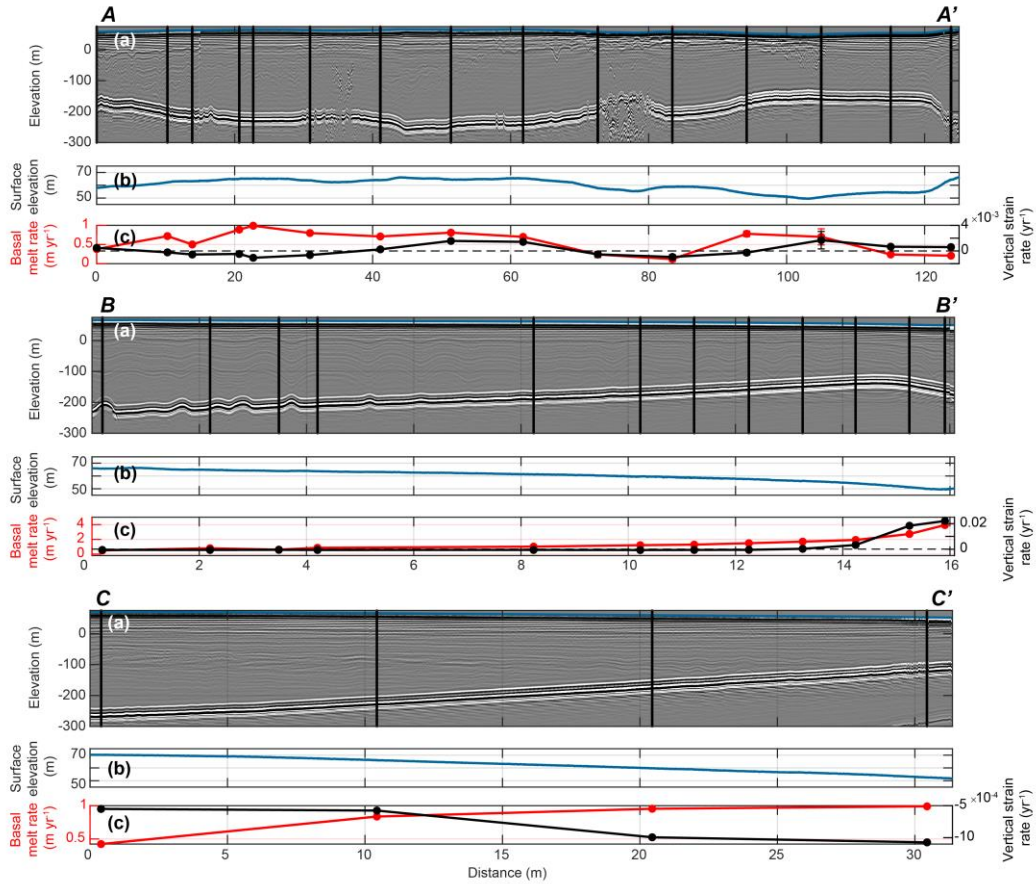
Figure 3. Profiles of low-frequency radar, ice surface elevation, basal melt, and strain (locations in Fig. 1b): A–A' across ice flow from west to east (125 km), B–B' along ice flow from south to north towards an ice rumple (16 km), and C–C' along ice flow from south to north out towards the ice front (32 km). Sub-panels show **(a)** radar profiles with surface elevation (blue line), englacial stratigraphy, and basal elevation (grey tone shading), and locations of ApRES measurements (black vertical lines), **(b)** surface elevation from carrier-phase kinematic GPS measurements, and **(c)** annual basal melt rate (red) and vertical strain rates (black, dashed = 0) for 2017. Note that the x-axis scales vary between the three profiles.

2b), possibly due to errors in the input data or the interpolation between them. Ice draft varied from 120 to 280 m with a median value of 220 m (Fig. 3). We observed no significant relation between basal melting and ice draft. Several locations with undulating englacial layers, basal channels and crevasses were visible in the radar profiles (Fig. 3). Stake-measured ice flow speeds varied from 13 to 113 m yr^{-1} in 2017, with an average value of 80 m yr^{-1}, agreeing with satellite estimates (Rignot et al., 2011; Fig. 2c). Surface mass balance values varied between 0.12 and

14

354 0.62 m i.e. yr^{-1} in 2017 with an average of 0.45 i.e. yr^{-1}, higher than the modelled average

355 estimates of 0.2 m i.e. yr^{-1} (van de Berg et al., 2006), but with the same spatial pattern (Fig. 2d).

356

357 **5   Discussion**

358   In the following sections, we discuss the spatial and temporal variations in basal melting

359 and compare our results with other studies from Antarctica. For each section, we also discuss

360 strengths, limitations, and recommendations for future studies.

361 5.1   Spatial variations in melting

362   On Nivlisen, we observed the highest averaged annual basal melt rates (3.9 m yr^{-1}) close

363 to a small (4.2 km^2) ice rumple at the ice front (Fig. 2a and Fig. 3). Similar basal melt rates (~4

364 m yr^{-1}) were inferred from satellite data nearby Bawden Ice Rise in the Antarctic Peninsula

365 (Adusumilli et al., 2018). In modelling experiments, locally enhanced basal melt rates were

366 caused by strong tidal currents in shallow regions (thin water column thickness) around the ice

367 rise that increased the ice-ocean heat exchange (Mueller et al., 2012). At Nivlisen, we have no

368 observations of ocean currents near the ice rumple, but the bathymetry must be shallow since the

369 ice shelf grounds in this region. Ice shelf thinning could potentially increase the water column

370 thickness, leading to a negative (stabilizing) feedback on the melting by reducing the ocean

371 currents (Mueller et al., 2012, 2018; Padman et al., 2018). In terms of ice thickness change, the

372 observed thinning from the basal melt is compensated by a positive vertical strain that implies

373 compressional thickening towards the ice rumple (up to 4 m yr^{-1}). Thicker ice towards the ice

374 rumple indicates a buttressing effect on the ice shelf (profile B; Fig. 3). We observed many

375 crevasses in this region that made it, for safety reasons, difficult to revisit the three closest sites

376 during the third field season (Dec 2018). Many ice shelves like Nivlisen are stabilized by pinning

377 points at their ice fronts, which may be sensitive areas for future change. The effects of an

378 increased basal melting in the future at the Nivlisen ice rumple are uncertain, and modelling

379 work may indicate whether un-grounding of the ice would potentially lead to substantial loss of

380 buttressing (Borstad et al., 2013).

15

381   Estimates of basal melt rates for Dronning Maud Land ice shelves have mainly used

382   satellite techniques, modelling, or limited spatial or temporal coverage of in situ radar

383   observations (Berger et al., 2017; Langley et al., 2014b). Fimbulisen is situated 400 km west of

384   Nivlisen (Fig. 1a) at the outlet of Jutulstraumen, one of the largest ice streams in Dronning Maud

385   Land. Below the deep keel from Jutulstraumen (300–400 m ice draft), time-averaged basal melt

386   rates of several meters per year were observed, whereas at the shallower parts of the ice shelf

387   (200–300 m ice draft), lower melt rates were observed (Langley et al., 2014a). In addition,

388   annual-average basal melt rates were modelled to be near zero for large areas (Hattermann et al.,

389   2014). Hattermann et al. (2014) hypothesized that basal melting (melt mode 1, Sect. 1) occurred

390   at the deepest parts of Fimbulisen (below ice drafts of 400 m). The rising melt plume caused

391   marine accretion at shallower depths closer to the ice front, which together with seasonal melting

392   from summer-heated surface water (melt mode 3, Sect. 1), resulted in the low net basal melt

393   rates. The seasonal marine-ice formation was inferred from an ice shelf cavity mooring

394   (Hattermann et al., 2012). Nivlisen is in comparison relatively thin (Fig. 2b) and we have no melt

395   observations from the thicker ice in the southern areas. Grounding line ice drafts (Fig. 1b),

396   derived from Fretwell et al. (2013) and Mouginot et al. (2017), have an average value of 350 m.

397   The deepest part of the grounding line (630 ± 100 m) is located at the outflow of Potsdam

398   Glacier (Fig 1b), where higher basal melt rates may occur. In addition, Nivlisen has three ice-

399   front sections, separated by ice rises and ice rumples, where the ocean can gain access to the

400   inner parts of the ice shelf cavity. At Fimbulisen, Hattermann et al. (2012, 2014) found that a

401   portion of the westward flowing coastal current was diverted under the ice shelf between two ice

402   rises. Similar inflow pathways may also exist beneath the ice-front sections of Nivlisen,

403   explaining the variations of basal melt rates along profile A (Fig. 2a). At Fimbulisen, higher

404   basal melt rates (3 m yr^{-1}) were also observed and modelled close to the ice front at shallow

405   depths (< 200 m; Hattermann et al., 2014; Langley et al., 2014b), which is consistent with our

406   results.

407   In the low-frequency radar profiles, we observed several undulating ice-base features

408   (profile A and B; Fig. 3), where the englacial layers warp downwards, which is likely an

409   indication of basal channels or crevasses. The southernmost measurement in profile B is located

410   at one of these down-warping features, where surface elevation is slightly lowered locally (−0.5

411   m). Higher basal melt rates were not observed here compared with the surrounding sites,

412   although, higher melt rates typically occur on the flanks of basal channels, rather than at their

413   apex (Berger et al., 2017). The channel may have formed at an upstream ice rumple and been

414   passively advected downstream (Fig. 2a). Basal channels are important features influencing the

415   ice-shelf stability, since they affect ice-shelf cavity circulation and play a role in the exchange of

416   heat and mass between the ocean and ice shelf (Gladish et al., 2012; McGrath et al., 2012;

417   Millgate et al., 2013; Stanton et al., 2013). Basal channels are not restricted to rapidly melting ice

418   shelves and have been observed elsewhere in Dronning Maud Land, at Fimbulisen (Langley et

419   al., 2014a) and Roi Baudouin Ice Shelf (Fig. 1a; Berger et al., 2017). Detailed studies of these

420   features together with basal melting are needed to understand their initiation, evolution, and role

421   in the overall mass balance of ice shelves (Alley et al., 2016).

422   5.2   Temporal variations in melting

423   Basal melt rates at Nivlisen varied on a broad range of timescales (Fig. 4 and 5). At the

424   seaward site, we observed a seasonal signal, where the monthly averaged basal melt rates were

425   two to three times higher in the summer than in winter (Fig. 4a, Supplements Fig. S3). At the

426   landward site, we observed no seasonal pattern, however, some variability on monthly time-

427   scales was present (Fig. 5a, Supplements Fig. S3). We performed a continuous wavelet transform

428   on the time-series data from the two overwintering sites, based on the method and software

429   package provided by Grinsted et al. (2004). The wavelet transform is used to study localized

430   intermittent periodicities, in contrast to more traditional mathematical methods, such as Fourier

431   analysis, which assumes that the underlying process is stationary in time. We used a Morlet

432   wavelet with $\omega_0 = 6$, which provides a good balance between time and frequency localization.

433   The wavelet transform shows the normalized thinning rates at different scales to identify

434   dominant periods of variability in time (Fig. 4b, 5b). The statistical significance was assessed

435   relative to the null hypothesis, modelled by a first order autoregressive process. The wavelet

436   transform has edge artefacts since it is not completely localized in time, as indicated by the cone

437   of influence, masking out low frequency signals at the beginning and end of the time series. The

438   thinning variability at diurnal timescales, and to some extent semi-diurnal timescales, varied at

439   an approximately two-weekly period. This reflects the fortnightly spring-neap tidal cycle at
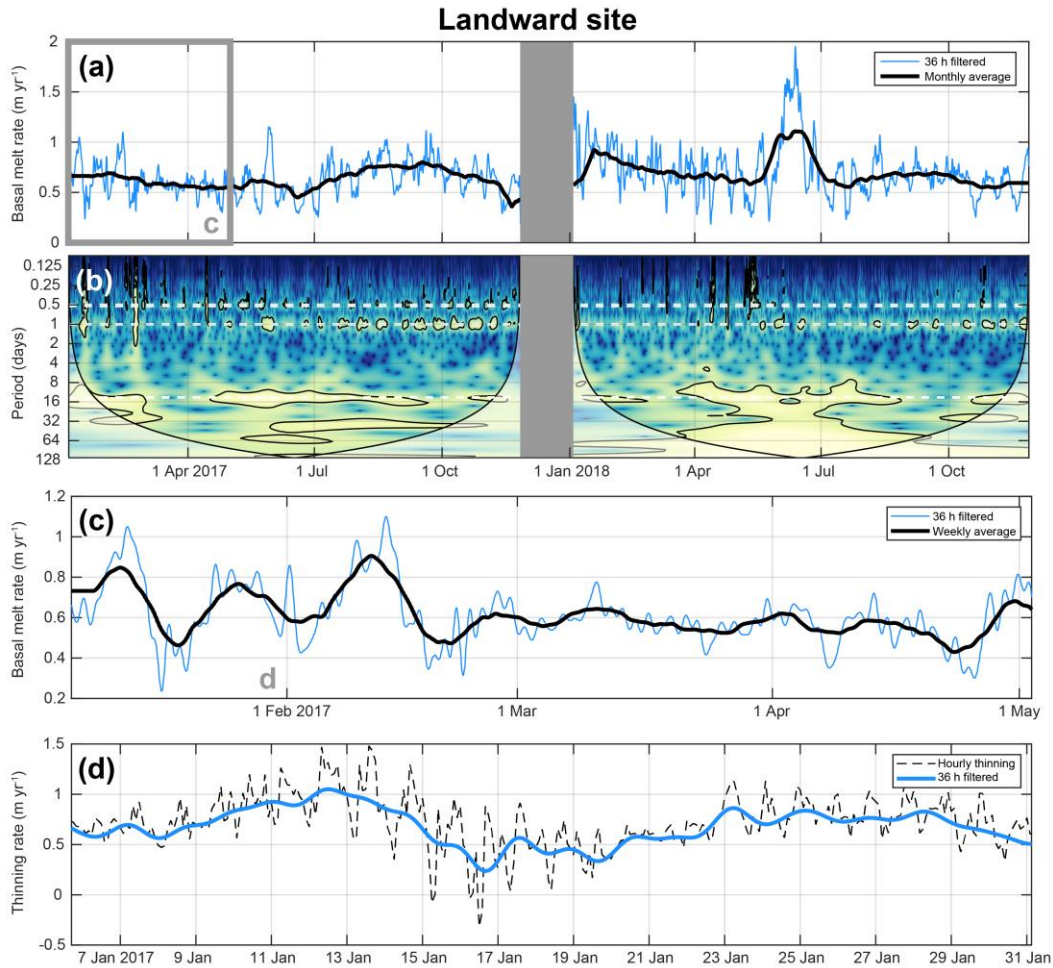
17
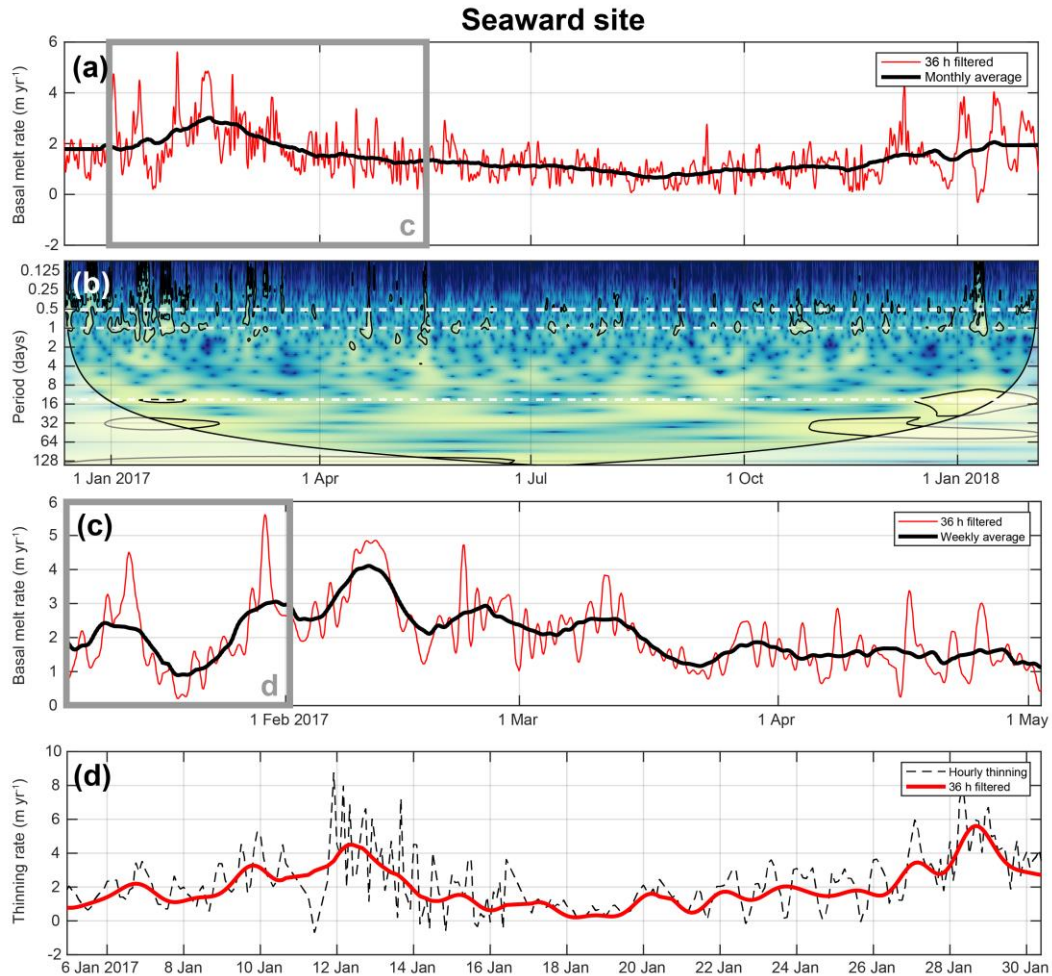
Figure 4. Basal melt and thinning rates for the seaward overwintering site, with variations on time scales of **(a)** months (11 Dec 2016–4 Feb 2018), **(c)** weeks (1 Jan–1 May 2017), and **(d)** days (1–31 Jan 2017). Dashed black line in (d) is the unfiltered raw data with thickness change including strain rates. **(b)** Continuous wavelet transform of the normalized thinning to identify the dominant modes of variability at different time scales. The left axis is the Fourier period. The colour shading represents the thinning associated with fluctuations over the course of the year with a particular time period (yellow = high power, blue = low power). The black contours delimit significant modes of variance at 95 % against red noise. Within the cone of influence, shown as a lighter shade in the right and left lower corners, edge effects may distort the image. Dashed white lines show the periods of major tidal constituents (0.5 d $\approx$ K_1, 1 d $\approx$ M_2/S_2, and 14 d $\approx$ M_f).

which the strength of the tidal currents varies because of the interference of different constituents, usually M_2 and S_2 in this area (plotted as white dashed lines in Fig. 4b and 5b). Stronger tidal currents increase the heat exchange at the ice-ocean interface and may hence cause

Figure 5. Basal melt and thinning rates for the landward overwintering site, with variations on time scales of **(a)** months (4 Jan 2017−27 Nov 2018), **(c)** weeks (4 Jan−1 May 2017), and **(d)** days (4−31 Jan 2017). **(b)** Continuous wavelet transform of the normalized thinning to identify the dominant modes of variability at different time scales. Grey box masks a time period with no data. See Fig. 4 caption for more information.

more rapid melt. At periods shorter than 36 hours, however, we cannot differentiate the strain signal from the melt signal. We also see some evidence of a slower variability in the data centred on 2−4 days (Fig. 4d and 5d), which may be a result of mesoscale activity passing by the site (eddies or internal waves), which then show up in the melt rate. This is to some extent supported by Fourier analysis of the normalized 36 h filtered basal melt rates, which show peaks in power spectral density at 2−4 days, mostly visible at the seaward site (Supplements Fig. S4).

466   At the landward site, we observed no increased melting in summer, but we observed one

467   melt peak in winter (12 June 2018; Fig. 5a). The melt event may have been caused by pulses of

468   modified warm deep water reaching the base of the ice shelf as described by Hattermann et al.

469   (2012), but it could also relate to other mesoscale activities within the cavity. In any case, the

470   isolated event and the generally low basal melt rates suggest that warm deep water had limited

471   access to the base of Nivlisen during 2017 and 2018. The observation is consistent with earlier

472   studies, showing that ice shelf cavities in this region are mainly filled with cold and fresh eastern

473   shelf water (Nicholls et al., 2006; Thompson et al., 2018). Many factors control the extent to

474   which warm deep water can access the ice shelf cavities in Dronning Maud Land, such as the

475   stability of the Antarctic slope front, local circulation, and bathymetry, and this has to be studied

476   in more detail.

477   We studied the coherency between the two overwintering melt sites in a wavelet

478   coherence (Grinsted et al., 2004) for the overlapping time periods in 2017 (Fig. 6). The wavelet

479   coherence analysis finds significant coherence even if the common power is low, and it shows

480   significant confidence levels against red noise backgrounds. Locally phase-locked behaviour can

481   also be revealed; at weekly to monthly periods (7−30 days) in summer to fall (Jan−Apr 2017) the

482   basal melt rates were in phase, whereas in winter (Apr−Jun) the melting at the seaward site led

483   the increased signal, preceding the melt at the landward site. In late winter (Sept), the phase

484   shifted to the landward site leading the melt. At Fimbulisen, the inflow of summer-warmed

485   Antarctic surface water was observed at moorings close to the ice shelf front with a clear

486   seasonal signal in water temperatures and salinity (Hattermann et al., 2012). Hattermann et al.

487   (2014) suggested that Antarctic surface water can reside for several months below the ice shelf

488   cavity, after initially being subducted beneath the ice front, potentially affecting basal melting

489   deep inside the cavity. The observed melt rate pattern beneath Nivlisen may be an indication of

490   similar movement of water masses below the ice shelf and further modelling is needed to study

491   these processes, currently being hampered by the lack of knowledge of bathymetry beneath the

492   ice shelf.

493   We compared the basal melt rates with atmospheric ERA5 reanalysis data of wind speed,

494   wind direction, air temperature, and sea-ice cover (Fig. 7) produced by the European Centre for

495   Medium-Range Weather Forecasts (Copernicus Climate Change Service (C3S), 2017) at a grid

20

496
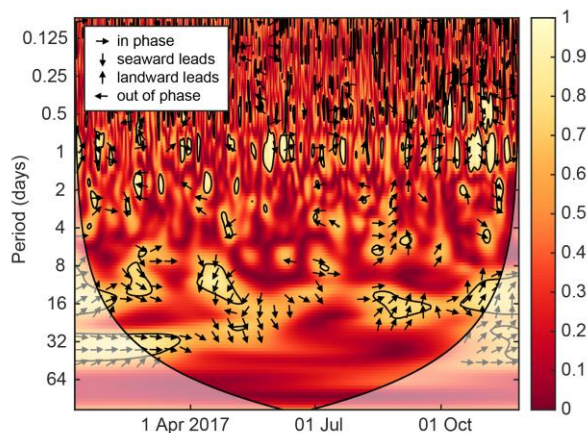
Figure 6. Wavelet coherence between overlapping time periods of the seaward and landward site (4 Jan–27 Nov

2017), showing times where the basal melt rates have common power. The phase relationship is shown as arrows. At

longer periods (8–30 days) in summer to fall (Jan–Apr) the signals are in phase, whereas in winter (Apr–Jun) the

melt at the seaward site leads the signal. In late winter (Sept) the phase shifts to the landward site leading the signal.

Within the cone of influence, shown as a lighter shade, edge effects become important.

502

point 10 km north of the ice shelf front (Fig. 1b). ERA5 wind speeds at Nivlisen varied on daily

timescales, ranging from 0 to 28 m s^{-1}. Winds generally blew from the east (Fig. 7b),

corresponding to the pressure gradients imposed by the cyclonic system that dominates the

Weddell Sea. As wind forcing can play an important role in downwelling and transportation of

summer-warmed Antarctic surface water into the ice-shelf cavity (Zhou et al., 2014). We

calculated the coherence between the normalized basal melt rates at the seaward site and wind

speeds during time periods when there was open water in front of the ice shelf (grey area in Fig.

7a). The statistical significance level was estimated using Monte Carlo simulation with a Fourier

transform method, where a large set of surrogate data set pairs were generated using phase

randomization (Schreiber and Schmitz, 2000). We found a significant coherence between basal

melt rates and wind speeds ($r = 0.35$, $p < 0.01$; Fig. 8). We found no such coherence in winter.

The variability in winter may be due to the transport mainly dominated by eddies, shed by

instabilities in the along-slope current. We also compared individual melt peaks in the summer

with higher wind events (dashed vertical lines in Fig. 7). The melt peaks have a time lag of ~0 to

3 days after a wind event. Air temperatures at 2 m varied mostly on seasonal time scales, with

21

518   temperatures between 0 and −10° C in summer, when we observe the highest basal melting, and

519   down to −28° C in winter (Fig. 7c). The temperature variability in the reanalysis data on shorter

520   timescales agreed with our weather station on Leningradkollen ice rise (190 m a.s.l.), however,

521   the seasonal temperature signal had a lower amplitude than at the weather station, which

522   measured temperatures down to −38° C. When air temperatures were high and basal melt rates

523   increased in early summer at the seaward site (Dec 2016 and 2017), we observed open water

524   close to Nivlisen, which is the time when solar radiation may warm the surface waters (Fig. 7).

525   Sea ice is widespread in front of the ice shelf during winter and then breaks up during summer

526   typically starting from the west and progressing to the more sheltered eastern side (Supplements

527   Fig. S5). The general pattern of summer retreat is interrupted by irregular periods of some sea ice

528   re-growth (e.g. early February 2017 and 2018; Fig. S5). Similar seasonally higher basal melt

529   rates (up to ~5 m yr^{-1}) were observed at Ross Ice Shelf in West Antarctica, where solar-heated

530   surface water in a polynya near the ice front was linked to the higher melt rates; however, they

531   did not find any link to downwelling-favourable winds, but rather density gradients caused by

532   seasonal brine release in the polynya (Stewart et al., 2019).

533
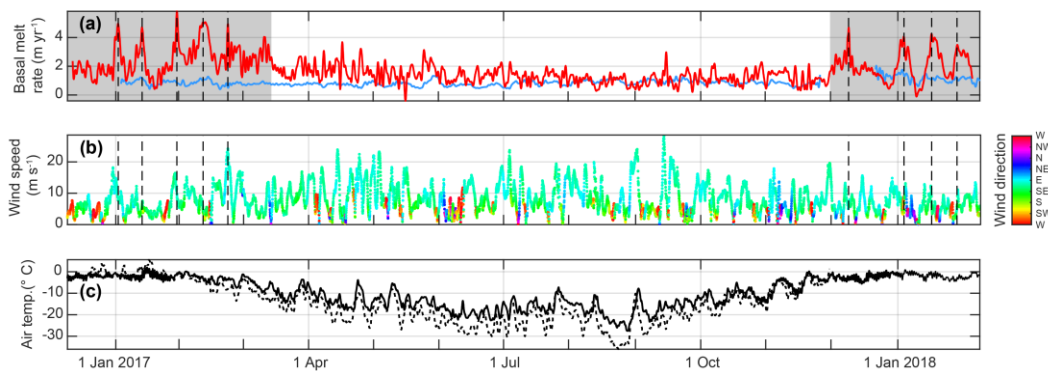
535   **Figure 7.** Basal melt rates compared with atmospheric forcing and sea-ice cover: **(a)** Thirty-six hour low-pass

536   filtered basal melt rates at seaward site (red) and landward site (blue). Shaded grey area represents the time period in

537   satellite data when there is open water in front of the ice shelf (Supplements Fig. S6). ERA5 reanalysis surface data

538   of **(b)** wind speed and direction and **(c)** 2 m air temperature, where dashed black line is data from a nearby weather

539   station (Fig. 1b). Vertical dashed lines show where time lags were calculated between basal melt and wind peaks.

540
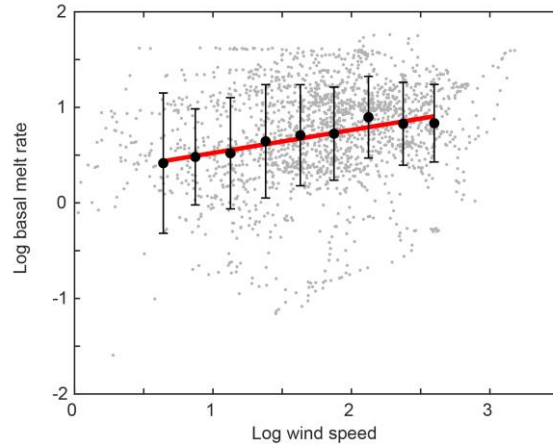
Figure 8. Scatter plot with the normalized basal melt rates at the seaward site and wind speeds for the time period when there was open water in front of the ice shelf (grey area in Fig. 7a). Black points show average basal melt rate calculated for each wind speed bin of 0.25 intervals. The red line shows the linear regression.

In summary, the basal melt rates varied on seasonal, monthly, and daily timescales related to the tidal cycles and mesoscale activities in the ice-shelf cavity. We hypothesize that summer-warmed Antarctic surface water was pushed by wind under the front of Nivlisen ice shelf. Reduced sea-ice cover and higher wind speeds may increase melting from surface waters, while weaker winds and/or changes in the surface buoyancy forcing may increase exposure of the sub ice-shelf cavities to warm deep water. Surface winds are projected to intensify over the next century with increased greenhouse gas emissions (Greene et al., 2017) and extreme changes in sea-ice extent have occurred in recent years (Shepherd et al., 2018). Warming of the surface water is projected to increase ice-shelf melting along Dronning Maud Land in future climate scenarios (Kusahara and Hasumi, 2013) and recent studies suggest that non-linear feedbacks may facilitate an irreversible transition into a state of higher melting in the Weddell Sea (Hattermann, 2018; Hellmer et al., 2017). Increases in basal melting will tend to thin the ice shelves and reduce the buttressing on the inland ice sheet. It remains to be understood to what extent, increased summer-warmth driven melting, intensified in the vicinity of pinning points may affect the ice flow dynamics and ice-shelf stability.

6   Conclusions

We present a two year record of basal melting at Nivlisen in Dronning Maud Land, East Antarctica, at high spatial and temporal resolution using in situ phase-sensitive radar measurements. Averaged annual basal melt rates are in general moderate (0.8 m yr^{-1}), but relatively high melt rates were observed close to a grounded feature near the ice shelf front. Hourly measurements also reveal a seasonal melt pattern close to the ice shelf front, where the highest basal melt rates occurred in summer (5.6 m yr^{-1}). Comparing the seasonality in basal melting with forcing from atmospheric reanalysis data, we found that the variability in the basal melt is likely caused by summer-warmed surface water pushed by the wind into the ice-shelf cavity. Farther into the ice-shelf cavity, we observe a different melt regime, with significantly lower basal melt rates and a clearer tidal signal. We conclude that warm deep ocean water has a limited effect on the basal melting of Nivlisen, likely because the present configuration of the Antarctic slope front, which separates the deeper water from the continent, protects the ice shelf from those warmer water masses. Our study highlights that, although many of the ice shelves in East Antarctica have generally low basal melt rates, their seaward sections have temporally higher basal melt rates due to the influence of summer-warmed surface waters. The frontal areas are stabilized by pinning points and these areas could potentially be sensitive to future change if the basal rates would increase. We demonstrate the use of and need for continuous in situ monitoring of Antarctic ice shelves to resolve variability in basal melting that is not captured in satellite data. Long-term, high-resolution time-series data are crucial to understand the complex mechanisms involved in ice shelf–ocean interactions.

Data availability

The compiled data sets of basal melt rates, strain rates, ice velocity, surface mass balance, and low-frequency radar profiles are available at the Norwegian Polar Data Centre (https://data.npolar.no).

Author contribution

KL led the overall data analysis and interpretations and prepared the paper with contributions from all co-authors. KL, GM, and BP collected the ApRES, ice flow speed, and surface mass balance in the field. KWN was responsible for the ApRES system setup. KM was responsible for the low-frequency radar system and collected the data in field. TH contributed to the discussion section. MT and KM were the project leaders.

Competing interests

KM is a member of the editorial board of the journal.

Acknowledgments

614 **References**

615 Adusumilli, S., Fricker, H. A., Siegfried, M. R., Padman, L., Paolo, F. S. and Ligtenberg,

616 S. R. M.: Variable Basal Melt Rates of Antarctic Peninsula Ice Shelves, 1994-2016, Geophys.

617 Res. Lett., 45, 4086–4095, doi:10.1002/2017GL076652, 2018.

618 Alley, K. E., Scambos, T. A., Siegfried, M. R. and Fricker, H. A.: Impacts of warm water

619 on Antarctic ice shelf stability through basal channel formation, Nat. Geosci., 9, 290, 2016.

620 Anschütz, H., Eisen, O., Oerter, H., Steinhage, D. and Scheinert, M.: Investigating small-

621 scale variations of the recent accumulation rate in coastal Dronning Maud Land , East Antarctica,

622 Ann. Glaciol., 46, 14–21, 2007.

623 Arndt, J. E., Schenke, H. W., Jakobsson, M., Nitsche, F. O., Buys, G., Goleby, B.,

624 Rebesco, M., Bohoyo, F., Hong, J., Black, J., Greku, R., Udintsev, G. and Barrios, F.: The

625 International Bathymetric Chart of the Southern Ocean (IBCSO) Version 1.0 — A new

626 bathymetric compilation covering circum-Antarctic waters, Geophys. Res. Lett., 40, 3111–3117,

627 doi:10.1002/grl.50413, 2013.

628 Bamber, J. L., Westaway, R. M., Marzeion, B. and Wouters, B.: The land ice contribution

629 to sea level during the satellite era, Environ. Res. Lett., 13, 2018.

630 van de Berg, W. J., van den Broeke, M. R., Reijmer, C. H. and van Meijgaard, E.:

631 Reassessment of the Antarctic surface mass balance using calibrated output of a regional

632 atmospheric climate model, J. Geophys. Res., 111, 1–15, doi:10.1029/2005JD006495, 2006.

633 Berger, S., Drews, R., Helm, V., Sun, S. and Pattyn, F.: Detecting high spatial variability

634 of ice-shelf basal mass balance, Roi Baudouin Ice Shelf, Antarctica, Cryosph., 11, 2675–2690,

635 doi:10.5194/tc-2017-41, 2017.

636 Bindschadler, R., Vornberger, P., Fleming, A., Fox, A., Mullins, J., Binnie, D., Jean, S.,

637 Granneman, B. and Gorodetzky, D.: Remote Sensing of Environment The Landsat Image Mosaic

638 of Antarctica, Remote Sens. Environ., 112(12), 4214–4226, doi:10.1016/j.rse.2008.07.006, 2008.

639 Borstad, C. P., Rignot, E., Mouginot, J. and Schodlok, M. P.: Creep deformation and

640 buttressing capacity of damaged ice shelves : theory and application to Larsen C ice shelf,

641 Cryosph., 7, 1931–1947, doi:10.5194/tc-7-1931-2013, 2013.

642   Brennan, P. V, Lok, L. B., Nicholls, K. and Corr, H.: Phase-sensitive FMCW radar

643   system for high-precision Antarctic ice shelf profile monitoring, IET Radar Sonar Navig., 8(7),

644   776–786, doi:10.1049/iet-rsn.2013.0053, 2014.

645   British Antarctic Survey: Instrument: Phase-sensitive radar (ApRES), Filchner Ice Shelf,

646   [online] Available from: https://www.bas.ac.uk/polar-operations/sites-and-

647   facilities/facility/phase-sensitive-radar-apres/ (Accessed 13 November 2018), 2018.

648   Copernicus Climate Change Service (C3S): ERA5: Fifth generation of ECMWF

649   atmospheric reanalyses of the global climate, Copernicus Clim. Chang. Serv. Clim. Data Store

650   [online] Available from: https://www.ecmwf.int/en/forecasts/datasets/reanalysis-datasets/era5

651   (Accessed 1 November 2018), 2017.

652   Corr, H. F. J., Jenkins, A., Nicholls, K. W. and Doake, C. S. M.: Precise measurement of

653   changes in ice-shelf thickness by phase-sensitive radar to determine basal melt rates, Geophys.

654   Res. Lett., 29(8), 1–4, 2002.

655   Darelius, E. and Sallée, J. B.: Seasonal Outflow of Ice Shelf Water Across the Front of

656   the Filchner Ice Shelf, Weddell Sea, Antarctica, Geophys. Res. Lett., 45, 3577–3585,

657   doi:10.1002/2017GL076320, 2017.

658   Davis, P. E. D., Jenkins, A., Nicholls, K. W., Brennan, P. V, Povl, E., Heywood, K. J.,

659   Dutrieux, P., Cho, K. and Wan, T.: Variability in Basal Melting Beneath Pine Island Ice Shelf on

660   Weekly to Monthly Timescales, J. Geophys. Res. Ocean., doi:10.1029/2018JC014464, 2018.

661   Depoorter, M. A., Bamber, J. L., Griggs, J. A., Lenaerts, J. T. M., Ligtenberg, S. R. M.,

662   Broeke, M. R. Van Den and Moholdt, G.: Calving fluxes and basal melt rates of Antarctic ice

663   shelves, Nature, 502(7469), 89–92, doi:10.1038/nature12567, 2013.

664   Dong, J., Speer, K. and Jullion, L.: The Antarctic Slope Current near 30 deg E, J.

665   Geophys. Res. Ocean., 121, 1051–1062, 2016.

666   Dowdeswell, J. A. and Evans, S.: Investigations of the form and flow of ice sheets and

667   glaciers using radio-echo sounding, Reports Prog. Phys., 67(10), 1821–1861, doi:10.1088/0034-

668   4885/67/10/R03, 2004.

669   Dupont, T. K. and Alley, R. B.: Assessment of the importance of ice-shelf buttressing to

670   ice-sheet flow, Geophys. Res. Lett., 32, 1–4, doi:10.1029/2004GL022024, 2005.

671   Fretwell, P., Pritchard, H. D., Vaughan, D. G., Bamber, J. L., Barrand, N. E., Bell, R.,
672   Bianchi, C., Bingham, R. G., Blankenship, D. D., Casassa, G., Catania, G., Callens, D., Conway,
673   H., Cook, A. J., Corr, H. F. J., Damaske, D., Damm, V., Ferraccioli, F., Forsberg, R., Fujita, S.,
674   Gim, Y., Gogineni, P., Griggs, J. A., Hindmarsh, R. C. A., Holmlund, P., Holt, J. W., Jacobel, R.
675   W., Jenkins, A., Jokat, W., Jordan, T., King, E. C., Kohler, J., Krabill, W., Riger-Kusk, M.,
676   Langley, K. A., Leitchenkov, G., Leuschen, C., Luyendyk, B. P., Matsuoka, K., Mouginot, J.,
677   Nitsche, F. O., Nogi, Y., Nøst, O. A., Popov, S. V, Rignot, E., Rippin, D. M., Rivera, A.,
678   Roberts, J., Ross, N., Siegert, M. J., Smith, A. M., Steinhage, D., Studinger, M., Sun, B., Tinto,
679   B. K., Welch, B. C., Wilson, D., Young, D. A., Xiangbin, C. and Zirizzotti, A.: Bedmap2:
680   improved ice bed, surface and thickness datasets for Antarctica, Cryosph., 7(1), 375–393,
681   doi:10.5194/tc-7-375-2013, 2013.

682   Gille, S. T.: Warming of the Southern Ocean Since the 1950s, Science, 295, 1275–1278,
683   2002.

684   Gingele, F. X., Kuhn, G., Maus, B., Melles, M. and Schöne, T.: Holocene ice retreat from
685   the Lazarev Sea shelf, East Antarctica, Cont. Shelf Res., 17(2), 137–163, 1997.

686   Gladish, C. V., Holland, D. M., Holland, P. R. and Price, S. F.: Ice-shelf basal channels in
687   a coupled ice/ocean model, J. Glaciol., 58(212), 1227–1244, doi:10.3189/2012JoG12J003, 2012.

688   Greene, C. A., Blankenship, D. D., Gwyther, D. E., Silvano, A. and Wijk, E. Van: Wind
689   causes Totten Ice Shelf melt and acceleration, Sci. Adv., 3, 1–5, doi:10.3934/mbe.2012.9.125,
690   2017.

691   Grinsted, A., Moore, J. C. and Jevrejeva, S.: Application of the cross wavelet transform
692   and wavelet coherence to geophysical time series, Nonlinear Process. Geophys., 11(5/6), 561–
693   566, doi:10.5194/npg-11-561-2004, 2004.

694   Hattermann, T.: Antarctic Thermocline Dynamics along a Narrow Shelf with Easterly
695   Winds, J. Phys. Oceanogr., 48, 2419–2442, doi:10.1175/JPO-D-18-0064.1, 2018.

696   Hattermann, T., Nøst, O. A., Lilly, J. M. and Smedsrud, L. H.: Two years of oceanic
697   observations below the Fimbul Ice Shelf, Antarctica, Geophys. Res. Lett., 39(L12605),

698   doi:10.1029/2012GL051012, 2012.

699   Hattermann, T., Smedsrud, L. H., Nøst, O. A., Lilly, J. M. and Galton-fenzi, B. K.: Eddy-
700   resolving simulations of the Fimbul Ice Shelf cavity circulation: Basal melting and exchange
701   with open ocean, Ocean Model., 82, 28–44, doi:10.1016/j.ocemod.2014.07.004, 2014.

702   Hazel, J. E. and Stewart, A. L.: Are the Near-Antarctic Easterly Winds Weakening in
703   Response to Enhancement of the Southern Annular Mode?, J. Clim., 32(6), 1895–1918,
704   doi:10.1175/jcli-d-18-0402.1, 2019.

705   Hellmer, H. ., Kauker, F., Timmermann, R. and Hattermann, T.: The Fate of the Southern
706   Weddell Sea Continental Shelf in a Warming Climate, J. Clim., 30, 4337–4350,
707   doi:10.1175/JCLI-D-16-0420.1, 2017.

708   Heywood, K. J., Locarnini, R. A., Frew, R. D., Dennis, P. F. and King, B. A.: Transport
709   and water masses of the Antarctic slope front system in the eastern Weddell Sea, Ocean. Ice,
710   Atmos. Interact. Antarct. Cont. Margin, 24(January), 203–214, doi:10.1029/ar075p0203, 1998.

711   Hogg, A. E. and Gudmundsson, G. H.: Impacts of the Larsen-C Ice Shelf calving event,
712   Nat. Clim. Chang., 7, 540–542, doi:10.1038/nclimate3359, 2017.

713   Horwath, M., Dietrich, R., Baessler, M., Nixdorf, U., Steinhage, D., Fritzsche, D.,
714   Damm, V. and Reitmayr, G.: Nivlisen, an Antarctic ice shelf in Dronning Maud Land: geodetic –
715   glaciological results from a combined analysis of ice thickness, ice surface height and ice-flow
716   observations, J. Glaciol., 52(176), 17–30, 2006.

717   Howat, I. M., Porter, C., Smith, B. E., Noh, M. J. and Morin, P.: The Reference Elevation
718   Model of Antarctica, Cryosph., 13, 665–674, doi:10.5194/tc-13-665-2019, 2019.

719   Irving, J. D., Knoll, M. D. and Knight, R. J.: Improving crosshole radar velocity
720   tomograms: A new approach to incorporating high-angle traveltime data, Geophysics, 72(4), 31–
721   41, doi:10.1190/1.2742813, 2007.

722   Jacobs, S. S., Helmer, H. H., Doake, C. S. M., A, J. and Frolich, R. M.: Melting of ice
723   shelves and the mass balance of Antarctica, J. Glaciol., 38(130), 375–387, 1992.

724   Jenkins, A. and Doake, C. S. M.: Ice-ocean interaction on Ronne Ice Shelf, Antarctica, J.

725   Geophys. Res. Ocean., 96(C1), 791–813, doi:10.1029/90JC01952, 1991.

726   Jenkins, A., Corr, H. F. J., Nicholls, K. W., Stewart, C. L. and Doake, C. S. M.:
727   Interactions between ice and ocean observed with phase-sensitive radar near an Antarctic ice-
728   shelf grounding line, J. Glaciol., 52(178), 325–346, 2006.

729   Joughin, I. and Vaughan, D. G.: Marine ice beneath the Filchner-Ronne Ice Shelf,
730   Antarctica: a comparison of estimated thickness distributions, Ann. Glaciol., 39, 511–517, 2004.

731   Kingslake, J., Ng, F. and Sole, A.: Modelling channelized surface drainage of
732   supraglacial lakes, J. Glaciol., 61(225), 185–199, doi:10.3189/2015JoG14J158, 2015.

733   Kusahara, K. and Hasumi, H.: Modeling Antarctic ice shelf responses to future climate
734   changes and impacts on the ocean Ž, J. Geophys. Res. Ocean., 118, 2454–2475,
735   doi:10.1002/jgrc.20166, 2013.

736   Kwok, R. and Comiso, J.: Southern Ocean Climate and Sea Ice Anomalies Associated
737   with the Southern Oscillation, J. Clim., 15, 487–501, 2002.

738   Kwok, R., Comiso, J. C., Lee, T. and Holland, P. R.: Linked trends in the South Pacific
739   sea ice edge and Southern Oscillation Index, J. Geophys. Res., 43, 295–302,
740   doi:10.1002/2016GL070655.Received, 2016.

741   Langley, K., von Deschwanden, A., Kohler, J., Sinisalo, A., Matsuoka, K., Hattermann,
742   T., Humbert, A., Nøst, O. A. and Isaksson, E.: Complex network of channels beneath an
743   Antarctic ice shelf, Geophys. Res. Lett., 41, 1209–1215, 2014a.

744   Langley, K., Kohler, J., Sinisalo, A., Øyan, M. J., Hamran, S. E., Hattermann, T.,
745   Matsuoka, K., Nøst, O. A. and Isaksson, E.: Low melt rates with seasonal variability at the base
746   of Fimbul Ice Shelf, East Antarctica, revealed by in situ interferometric radar measurements,
747   Geophys. Res. Lett., 41(22), 8138–8146, doi:10.1002/2014GL061782, 2014b.

748   Lapazaran, J. J., Otero, J. and Navarro, F. J.: On the errors involved in ice-thickness
749   estimates I: ground- penetrating radar measurement errors, J. Glaciol., 1–13,
750   doi:10.1017/jog.2016.93, 2016.

751   Lenaerts, J. T. M., Brown, J., Broeke, M. R. V. A. N. D. E. N., Matsuoka, K., Drews, R.,

752 Callens, D., Philippe, M., Gorodetskaya, I. V, Meijgaard, E. V. A. N., Reijmer, C. H., Pattyn, F.

753 and Lipzig, N. P. M. V. A. N.: High variability of climate and surface mass balance induced by

754 Antarctic ice rises, J. Glaciol., 60(224), 1101–1110, doi:10.3189/2014JoG14J040, 2014.

755 Lenaerts, J. T. M., Lhermitte, S., Drews, R., Ligtenberg, S. R. M., Berger, S. and Helm,

756 V.: Meltwater produced by wind – albedo interaction stored in an East Antarctic ice shelf, Nat.

757 Clim. Chang., 7, 58–63, doi:10.1038/NCLIMATE3180, 2017.

758 Lindbäck, K., Pettersson, R., Doyle, S. H., Helanow, C., Jansson, P., Kristensen, S. S.,

759 Stenseng, L., Forsberg, R. and Hubbard, A. L.: High-resolution ice thickness and bed topography

760 of a land-terminating section of the Greenland Ice Sheet, Earth Syst. Sci. Data, 6, 331–338,

761 doi:doi:10.5194/essd-6-331-2014, 2014.

762 Lindbäck, K., Kohler, J., Pettersson, R., Nuth, C. and Langley, K.: Subglacial

763 topography, ice thickness, and bathymetry of Kongsfjorden, northwestern Svalbard, Earth Syst.

764 Sci. Data, 10, 1769–1781, 2018.

765 Makinson, K. and Nicholls, K. W.: Modeling tidal currents beneath Filchner-Ronne Ice

766 Shelf and on the adjacent continental shelf: Their effect on mixing and transport, J. Geophys.

767 Res. Ocean., 104(C6), 13449–13465, doi:10.1029/1999jc900008, 1999.

768 Malyarenko, A., Robinson, N. J., Williams, M. J. M. and Langhorne, P. J.: A wedge

769 mechanism for summer surface water inflow into the Ross Ice Shelf cavity, J. Geophys. Res.

770 Ocean., 1196–1214, doi:10.1029/2018jc014594, 2019.

771 Marsh, O. J., Fricker, H. A., Siegfried, M. R., Christianson, K., Nicholla, K. W., Corr, H.

772 F. J. and Catania, G.: High basal melting forming a channel at the grounding line of Ross Ice

773 Shelf, Antarctica, Geophys. Res. Lett., 43, 1–6, doi:10.1002/2015GL066612.Received, 2016.

774 Matsuoka, K., Pattyn, F., Callens, D. and Conway, H.: Radar characterization of the basal

775 interface across the grounding zone of an ice-rise promontory in East Antarctica, Ann. Glaciol.,

776 53(60), 29–34, doi:10.3189/2012AoG60A106, 2012.

777 McGrath, D., Steffen, K., Scambos, T., Rajaram, H., Casassa, G. and Rodriguez Lagos, J.

778 L.: Basal crevasses and associated surface crevassing on the Larsen C ice shelf, Antarctica, and

779 their role in ice-shelf instability, Ann. Glaciol., 53(60), 10–18, doi:10.3189/2012AoG60A005,

780 2012.

781 Millgate, T., Holland, P. R., Jenkins, A. and Johnson, H. L.: The effect of basal channels

782 on oceanic ice-shelf melting, J. Geophys. Res. Ocean., 118(September), 6951–6964,

783 doi:10.1002/2013JC009402, 2013.

784 Moholdt, G. and Matsuoka, K.: Inventory of Antarctic ice rises and rumples (version 1), ,

785 doi:10.21334/npolar.2015.9174e644, 2015.

786 Mouginot, J., Scheuchl, B. and Rignot., E.: MEaSUREs Antarctic Boundaries for IPY

787 2007-2009 from Satellite Radar, Version 2., NASA Natl. Snow Ice Data Cent. Distrib. Act.

788 Arch. Center., doi:https://doi.org/10.5067/AXE4121732AD, 2017.

789 Mueller, R. D., Padman, L., Dinniman, M. S., Erofeeva, S. Y., Fricker, H. A. and King,

790 M. A.: Impact of tide-topography interactions on basal melting of Larsen C Ice Shelf, Antarctica,

791 J. Geophys. Res. Ocean., 117(5), 1–20, doi:10.1029/2011JC007263, 2012.

792 Mueller, R. D., Hattermann, T., Howard, S. L. and Padman, L.: Tidal influences on a

793 future evolution of the Filchner-Ronne Ice Shelf cavity in the Weddell Sea, Antarctica, Cryosph.,

794 12(2), 453–476, doi:10.5194/tc-12-453-2018, 2018.

795 Natural Resources Canada: CSRS-PPP: On-Line GNSS PPP Post-Processing Service,

796 [online] Available from: http://webapp.geod.nrcan.gc.ca/geod/tools-outils/ppp.php, 2017.

797 Nicholls, K. W., Abrahamsen, E. P., Buck, J. J. H., Dodd, P. A., Goldblatt, C., Griffiths,

798 G., Heywood, K. J., Hughes, N. E., Kaletzky, A., Mcphail, S. D., Millard, N. W., Oliver, K. I. C.,

799 Perrett, J., Price, M. R., Pudsey, C. J., Saw, K., Stansfield, K., Stott, M. J., Wadhams, P., Webb,

800 A. T. and Wilkinson, J. P.: Measurements beneath an Antarctic ice shelf using an autonomous

801 underwater vehicle, Geophys. Res. Lett., 33, doi:10.1029/2006GL025998, 2006.

802 Nicholls, K. W., Corr, H. F. J., Stewart, C. L., Lok, L. B., Brennan, P. V and Vaughan, D.

803 G.: Instruments and Methods A ground-based radar for measuring vertical strain rates and time-

804 varying basal melt rates in ice sheets and shelves, J. Glaciol., 61(230), 1079–1087,

805 doi:10.3189/2015JoG15J073, 2015.

806 Nøst, O. A., Biuw, M., Tverberg, V., Lydersen, C., Hattermann, T., Zhou, Q., Smedsrud,

807 L. H. and Kovacs, K. M.: Eddy overturning of the Antarctic Slope Front controls glacial melting

808   in the Eastern Weddell Sea, J. Geophys. Res. Ocean., 116(11), 1–17,

809   doi:10.1029/2011JC006965, 2011.

810   Padman, L., Siegfried, M. R. and Fricker, H. A.: Ocean Tide Influences on the Antarctic

811   and Greenland Ice Sheets, Rev. Geophys., 56(1), 142–184, doi:10.1002/2016RG000546, 2018.

812   Paolo, F. S., Fricker, H. A. and Padman, L.: Volume loss from Antarctic ice shelves is

813   accelerating, Science, 348(6232), 327–332, 2015.

814   Pritchard, H. D., Ligtenberg, S. R. M., Fricker, H. A., Vaughan, D. G., Broeke, M. R.

815   Van Den and Padman, L.: Antarctic ice-sheet loss driven by basal melting of ice shelves, Nature,

816   484(7395), 502–505, doi:10.1038/nature10968, 2012.

817   Rahman, S.: FMCW Radar Signal Processing for Antarctic Ice Shelf Profiling and

818   Imaging, Unversity College London., 2016.

819   Reese, R., Gudmundsson, G. H., Levermann, A. and Winkelmann, R.: The far reach of

820   ice-shelf thinning in Antarctica, Nat. Clim. Chang., 8, 53–57, doi:10.1038/s41558-017-0020-x,

821   2018.

822   Rignot, E., Mouginot, J. and Scheucht, B.: Ice Flow of the Antarctic Ice Sheet, Science,

823   333(September), 1427–1431, 2011.

824   Rignot, E., Jacobs, S., Mouginot, J. and Scheuchl, B.: Ice-Shelf Melting Around

825   Antarctica, Science, 341, 266–270, 2013.

826   Rignot, E., Mouginot, J., Scheuchl, B., van den Broeke, M. R., van Wessem, M. J. and

827   Morlighem, M.: Four decades of Antarctic Ice Sheet mass balance from 1979-2017, Proc. Natl.

828   Acad. Sci., 1–9, doi:10.1073/pnas.1812883116, 2019.

829   Rintoul, S. R., Silvano, A., Pena-molino, B., Wijk, E. Van, Rosenberg, M., Greenbaum,

830   J. S. and Blankenship, D. D.: Ocean heat drives rapid basal melt of the Totten Ice Shelf, Sci.

831   Adv., 2, 1–5, 2016.

832   Ryan, S., Schröder, M., Huhn, O. and Timmermann, R.: On the warm inflow at the

833   eastern boundary of the Weddell Gyre, Deep. Res. Part I Oceanogr. Res. Pap., 107, 70–81,

834   doi:10.1016/j.dsr.2015.11.002, 2016.

835   De Santis, A., Maier, E., Gomez, R. and Gonzalez, I.: Antarctica, 1979–2016 sea ice

836 extent: total versus regional trends, anomalies, and correlation with climatological variables, Int.

837 J. Remote Sens., 38(24), 7566–7584, doi:10.1080/01431161.2017.1363440, 2017.

838   Schmidtko, S., Heywood, K. J., Thompson, A. F. and Aoki, S.: Multidecadal warming of

839 Antarctic waters: Supplementary Material, Science, 346(6214), 1227–1231,

840 doi:10.1126/science.1256117, 2014.

841   Schreiber, T. and Schmitz, A.: Surrogate time series, Phys. D, 142, 346–382, 2000.

842   Shepherd, A., Fricker, H. A. and Farrell, S. L.: Trends and connections across the

843 Antarctic cryosphere, Nature, 558, 223–232, 2018.

844   Stanton, T. P., Shaw, W. J., Truffer, M., Corr, H. F. J., Peters, L. E., Riverman, K. L.,

845 Bindschadler, R. A., Holland, D. M. and Anandakrishnan, S.: Channelized Ice Melting in the,

846 Science, 341(September), 1236–9, doi:10.1126/science.1239373, 2013.

847   Stern, A. A., Dinniman, M. S., Zagorodnov, V., Tyler, S. W. and Holland, D. M.:

848 Intrusion of warm surface water beneath the McMurdo ice shelf, Antarctica, J. Geophys. Res.

849 Ocean., 118(12), 7036–7048, doi:10.1002/2013JC008842, 2013.

850   Stewart, A. L. and Thompson, A. F.: Eddy Generation and Jet Formation via Dense

851 Water Outflows across the Antarctic Continental Slope, J. Phys. Oceanogr., 46(12), 3729–3750,

852 doi:10.1175/jpo-d-16-0145.1, 2016.

853   Stewart, C. L., Christoffersen, P., Nicholls, K. W., Williams, M. J. M. and Dowdeswell,

854 J. A.: Basal melting of Ross Ice Shelf from solar heat absorption in an ice-front polynya, Nat.

855 Geosci., 1(January), doi:10.1038/s41561-019-0356-0, 2019.

856   Stuecker, M., Bitz, C. and Armour, K.: Conditions leading to the unprecedented low

857 Antarctic sea ice extent during the 2016 austral spring season, Geophys. Res. Lett., 44, 9008–

858 9019, doi:10.1002/2017GL074691.Received, 2017.

859   Sverdrup, H. U.: The Currents off the Coast of Queen Maud Land, Nor. Geogr. Tidsskr. -

860 Nor. J. Geogr., 14(1–4), 239–249, doi:10.1080/00291955308542731, 1954.

861   Swart, N. C., Gille, S. T., Fyfe, J. C. and Gillett, N. P.: Recent Southern Ocean warming

862 and freshening driven by greenhouse gas emissions and ozone depletion, Nat. Geosci., 11, 836–
863 842, doi:10.1038/s41561-018-0226-1, 2018.

864 Taylor, J. R.: An Introduction to Error Analysis: The Study of Uncertainties in Physical
865 Measurements, University of Colorado., 1996.

866 The IMBIE Team: Mass balance of the Antarctic Ice Sheet from 1992 to 2017, Nature,
867 558, 219–222, doi:10.1017/cbo9780511535659.014, 2018.

868 Thompson, A. F., Heywood, K. J., Schmidtko, S. and Stewart, A. L.: Eddy transport as a
869 key component of the Antarctic overturning circulation, Nat. Geosci., 7(12), 879–884,
870 doi:10.1038/ngeo2289, 2014.

871 Thompson, A. F., Stewart, A. L., Spence, P. and Heywood, K. J.: The Antarctic Slope
872 Current in a Changing Climate, Rev. Geophys., 56(4), 741–770, doi:10.1029/2018RG000624,
873 2018.

874 Turner, J., Hosking, J. S., Bracegirdle, T. J., Marshall, G. J. and Phillips, T.: Recent
875 changes in Antarctic Subject Areas, Philos. Trans. R. Soc. London, A 373(20140163), 2015.

876 Vaňková, I., Voytenko, D., Nicholls, K. W., Xie, S., Parizek, B. R. and Holland, D. M.:
877 Vertical Structure of Diurnal Englacial Hydrology Cycle at Helheim Glacier, East Greenland,
878 Geophys. Res. Lett., 45(16), 8352–8362, doi:10.1029/2018GL077869, 2018.

879 Zhou, Q., Hattermann, T., Nøst, O. A., Biuw, M., Kovacs, K. M. and Lydersen, C.:
880 Wind-driven spreading of fresh surface water beneath ice shelves in the Eastern Weddell Sea, J.
881 Geophys. Res. Ocean., 3818–3833, 2014.

882